Electronic Supplementary Information (ESI) for:

In silico free energy predictions for ionic liquid-assisted exfoliation of a graphene bilayer into individual graphene nanosheets

Ganesh Kamath and Gary A. Baker*

Department of Chemistry, University of Missouri–Columbia, Columbia, MO 65211.
Tel: 573–882–1811; E–mail: bakergar@missouri.edu

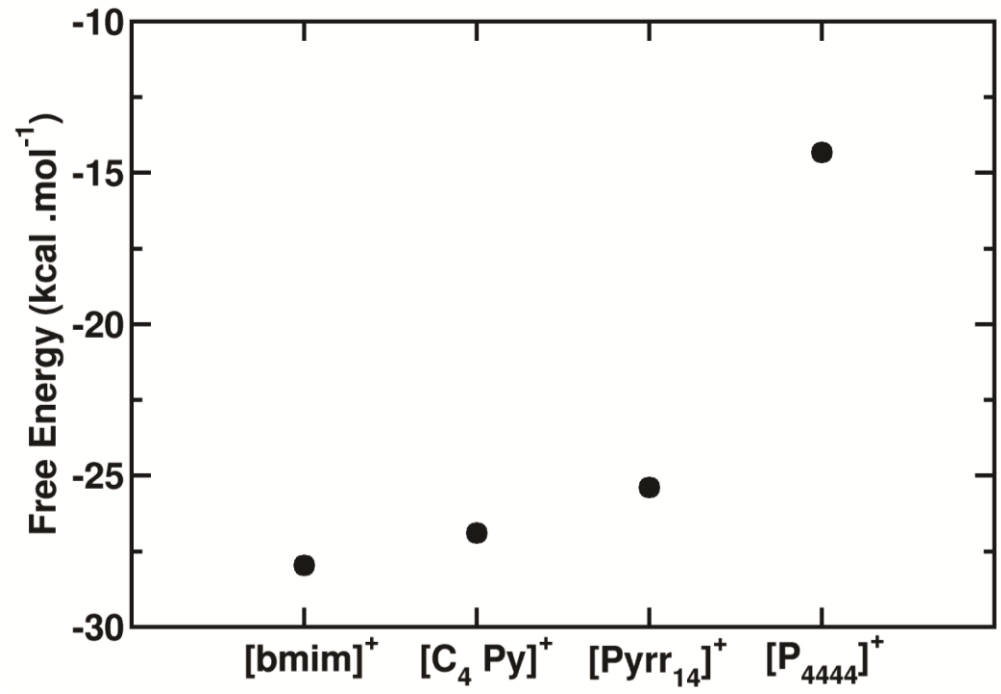

Fig. S1 Cation-dependent free energies of exfoliation for a graphene monolayer in various bis(trifluoromethylsulfonyl)imide $[NTf_2]^-$ based ILs, as predicted by ABF–MD simulations. For the molecular structures of the individual ions, see Fig. 1.

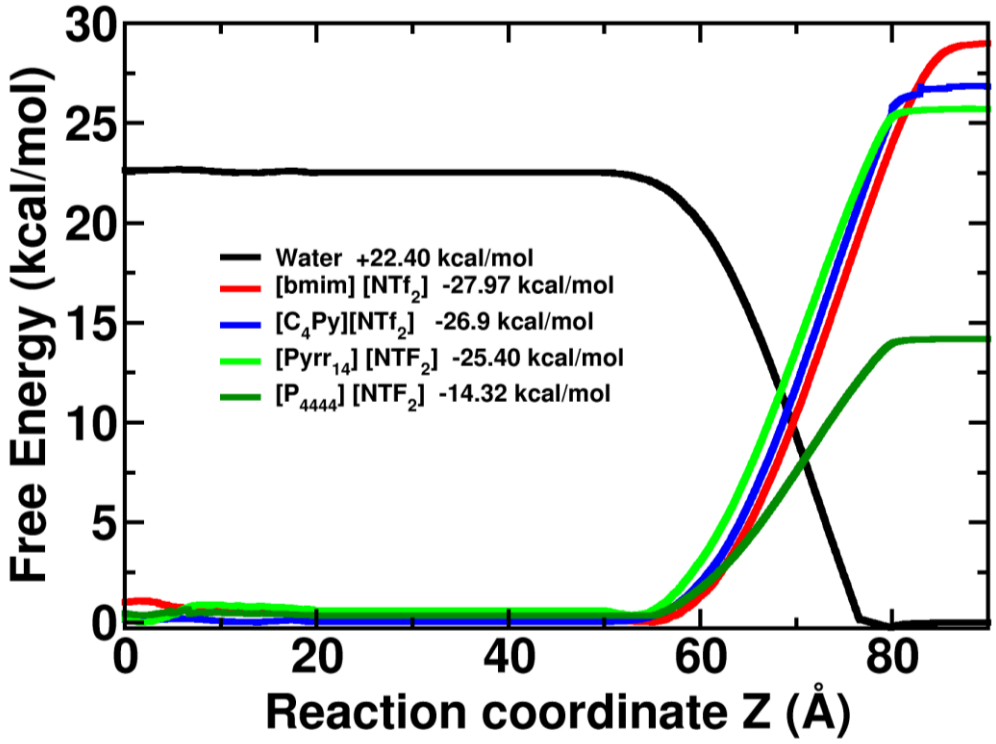

Fig. S2 Free energy of solvation profiles generated *via* ABF–MD for a graphene monolayer transferred from four different IL-rich phases to vacuum. Eighteen (18) windows of 5 Å bin width each in the z direction were used to compute the free energy change.

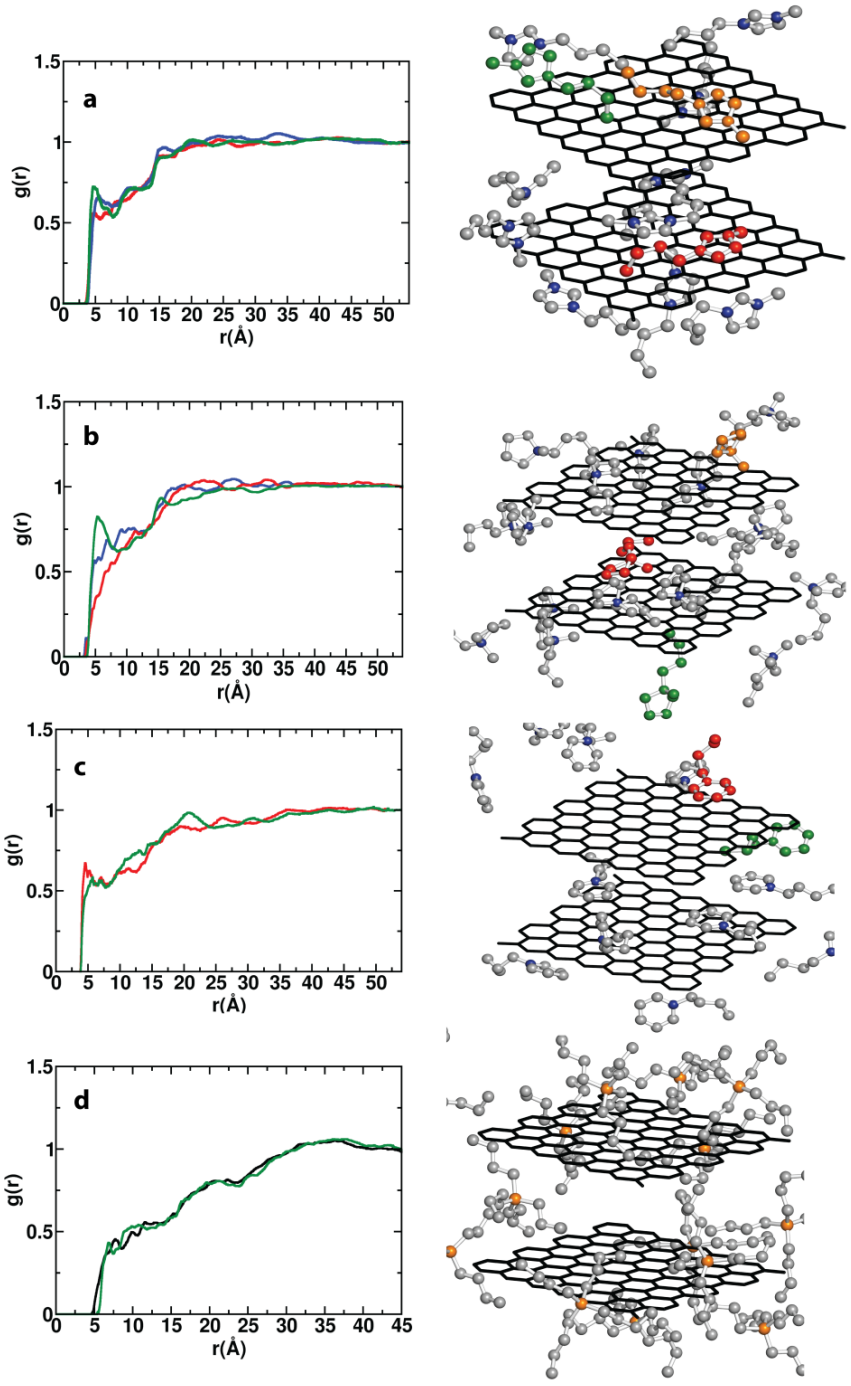

Fig. S3 IL cation interactions with graphene: a) $[bmim]^+$, b) $[Pyrr_{14}]^+$, c) $[C_4Py]^+$, and d) $[P_{4444}]^+$. Left Panel: RDFs of the methyl carbon (blue curve), butyl center of mass (green curve), and (where applicable) the ring (red curve) with graphene surface. Right: Snapshots of the interactions of different cations with the graphene bilayer. The hydrogens have been removed for clarity, whilst the carbons in $[bmim]^+$, $[Pyrr_{14}]^+$, $[C_4Py]^+$, and $[P_{4444}]^+$ are shaded grey. (d) The phosphorous interactions with graphene in the RDF are shown in black (left panel). Panels (a)–(c) are replicated from Fig. 3 for ease of comparison with $[P_{4444}][NTf_2]$.

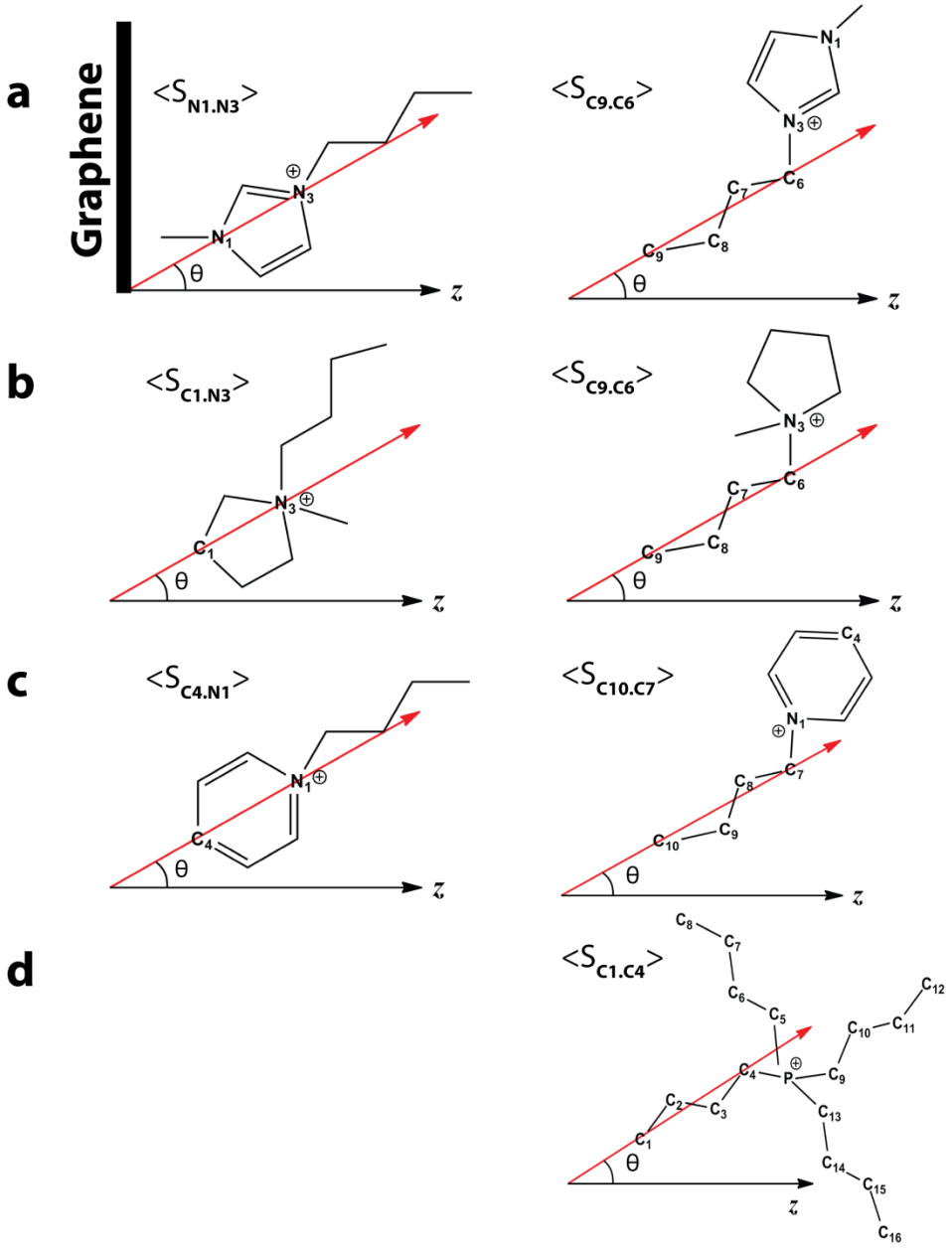

Fig. S4 Definition of the θ angle used to describe the orientation of the a) $[bmim]^+$, b) $[Pyrr_{14}]^+$, c) $[C_4Py]^+$, and d) $[P_{4444}]^+$ cations with respect to the *z* axis which extends normal to the graphene surface. The left panel illustrates the cation ring orientation with respect to the *z* axis and the right panel defines the orientation of the butyl chain in each cation. The ordering parameter corresponding to the angle θ is given by $\langle S \rangle = 1.5 \cos^2\theta - 0.5$.

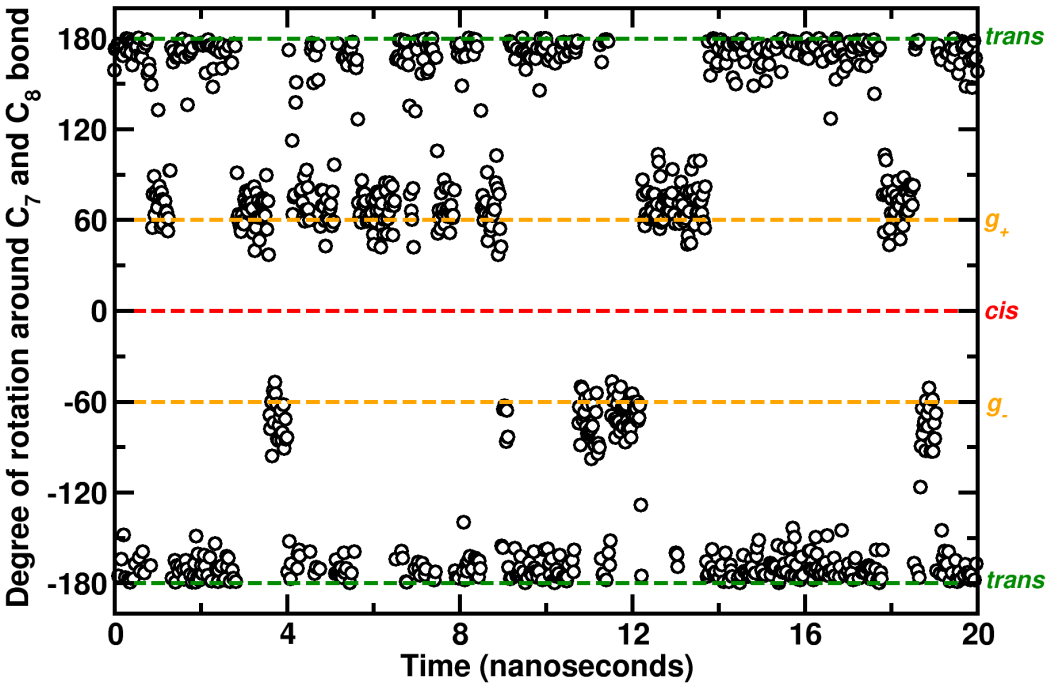

Fig. S5 Rotation about the C_7–C_8 bond in the butyl chain of $[bmim]^+$ (defined in Fig. S4) interacting with the graphene surface as the simulation proceeds. The butyl chain generally adopts a *trans* (anti) configuration but there exists a small energy barrier to rotation around the center bond, resulting in rapid interconversion between the gauche ($\langle g_+ \rangle$ or $\langle g_- \rangle$) conformers. Notably, high-energy eclipsed or *cis* conformations (+120, 0, and –120°) are demonstrably absent.

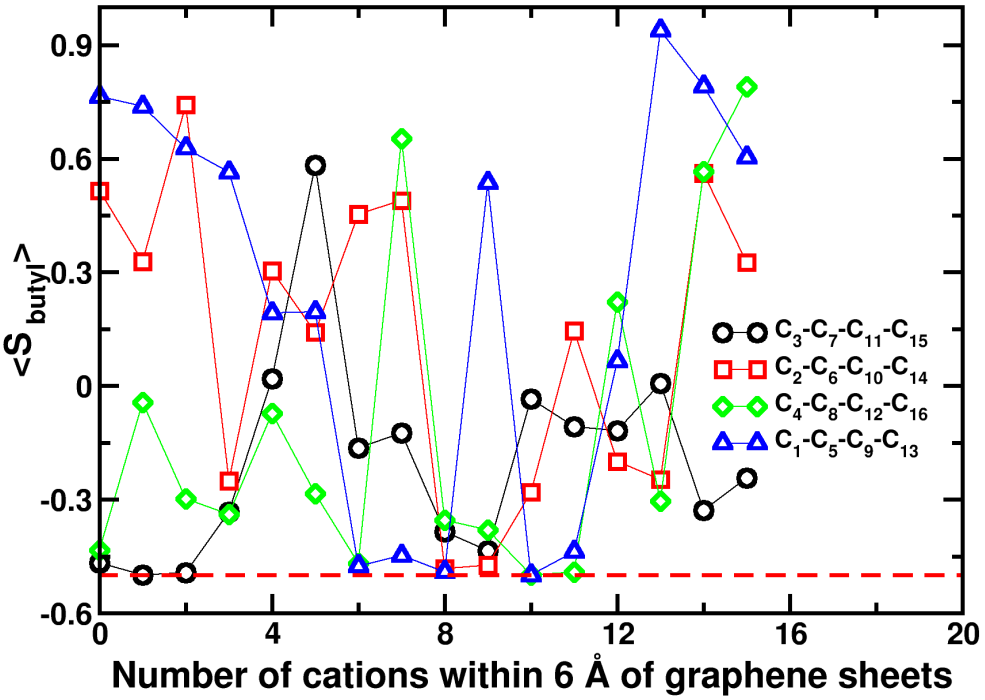

Fig. S6 The ordering parameter for the four equivalent butyl chains in the $[P_{4444}]^+$ cation with respect to the graphene surface.

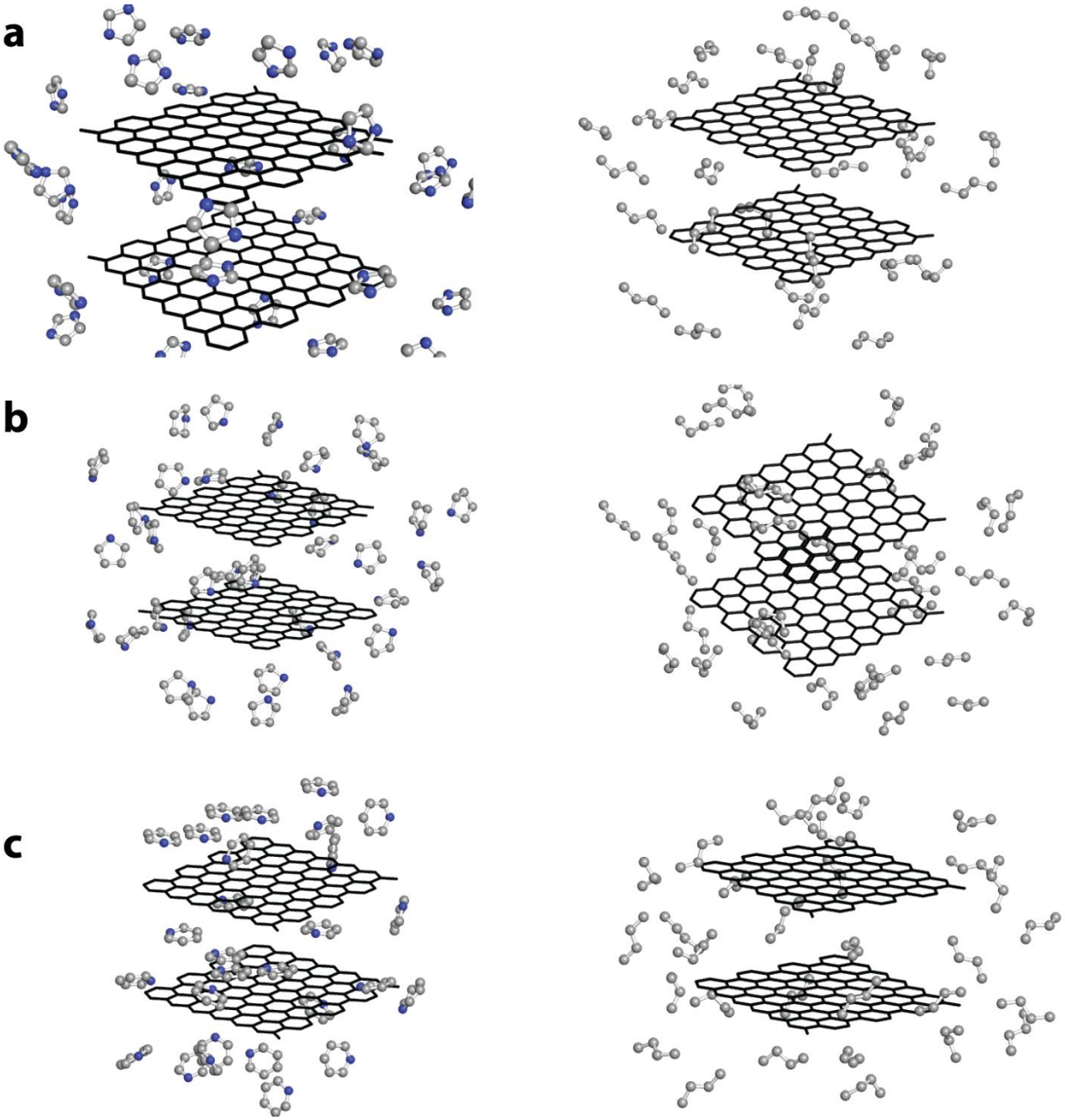

Fig. S7 (Left) Snapshots of cation interactions with graphene displaying only the ring structures for: a) $[bmim]^+$, b) $[Pyrr_{14}]^+$, and c) $[C_4Py]^+$. For $[bmim]^+$, there are relatively few rings parallel to the graphene sheet. A non-preferential orientation of the ring is seen for $[Pyrr_{14}]^+$ interactions with graphene. In contrast, a significant number of $[C_4Py]^+$ rings lie parallel to the graphene surface. (Right) Snapshots of butyl chain interactions with graphene for a) $[bmim]^+$, b) $[Pyrr_{14}]^+$, and c) $[C_4Py]^+$. In this projection, only the butyl chains are shown for clarity. Generally, a majority of the butyl chains adopt a *trans* configuration with *gauche* conformations being observed as well.

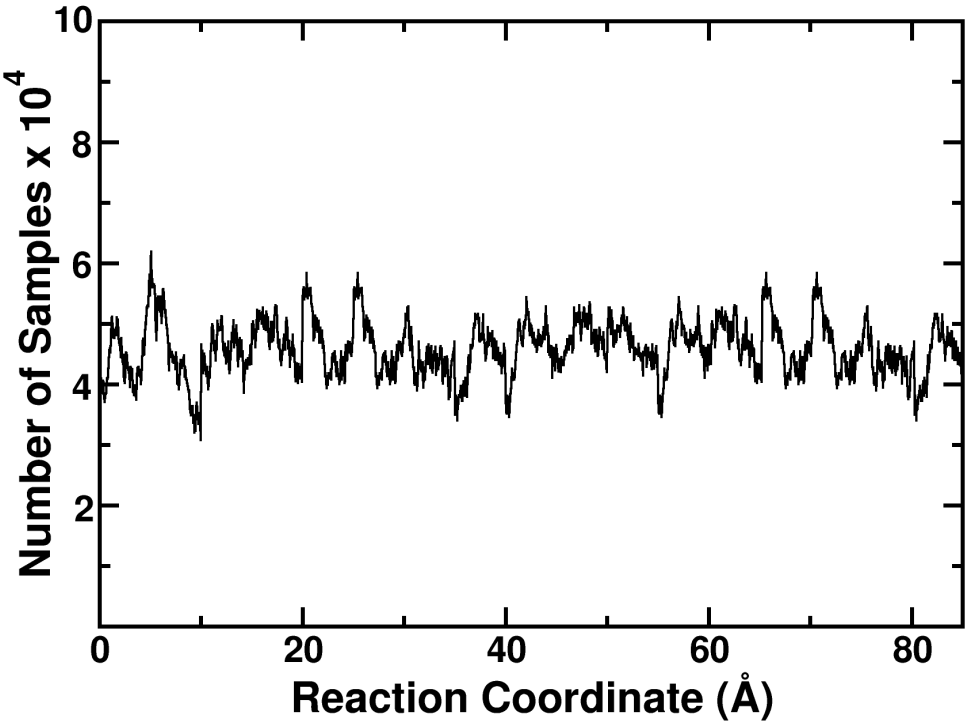

Fig. S8 Distribution of samples along the reaction coordinate from a 30 ns ABF–MD simulation of the transfer of a graphene sheet from [bmim][NTf_2] to vacuum.

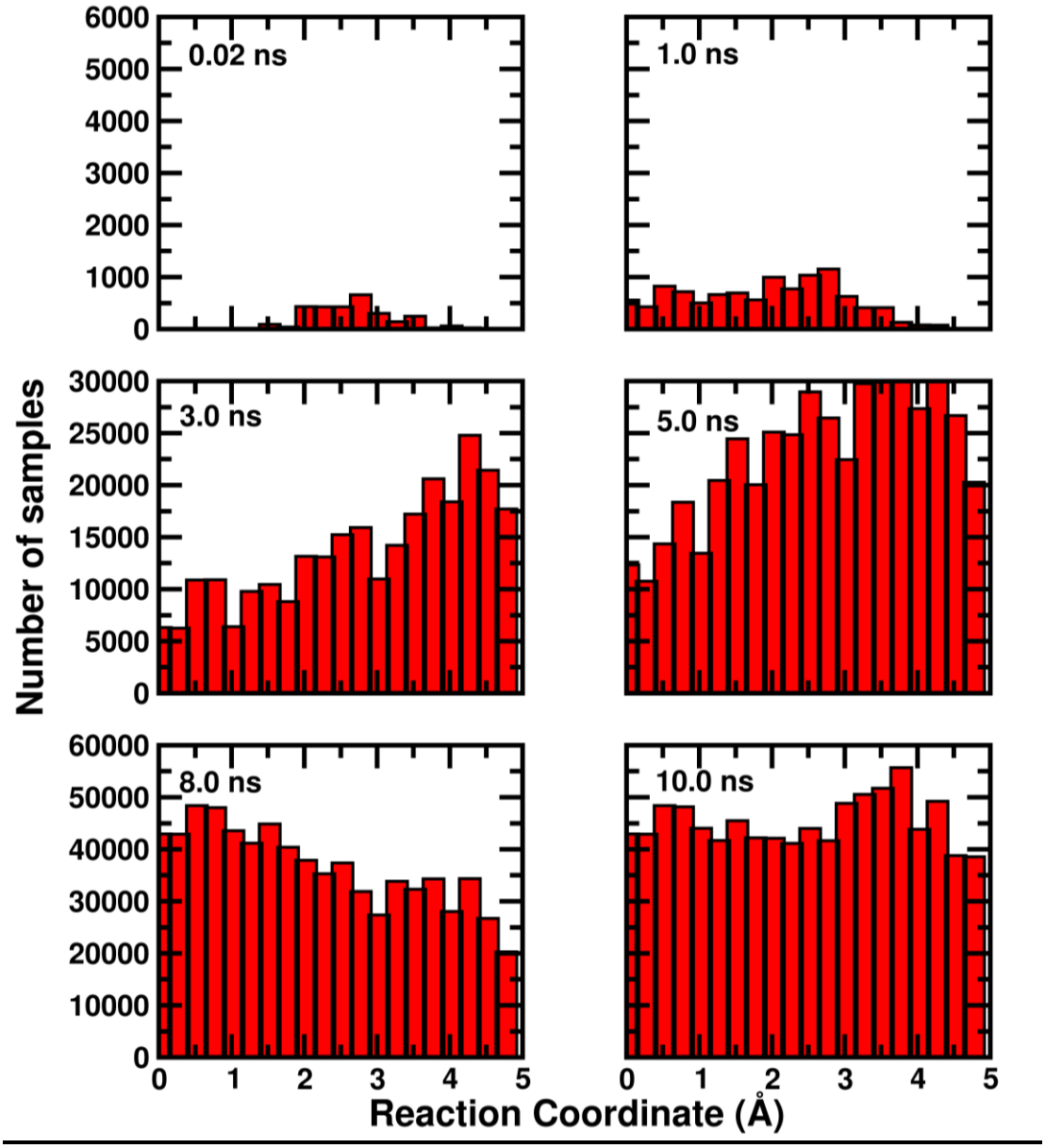

Fig. S9 Evolution of the sampling histogram from 0.02 to 10.0 ns during a 30.0 ns ABF–MD simulation.

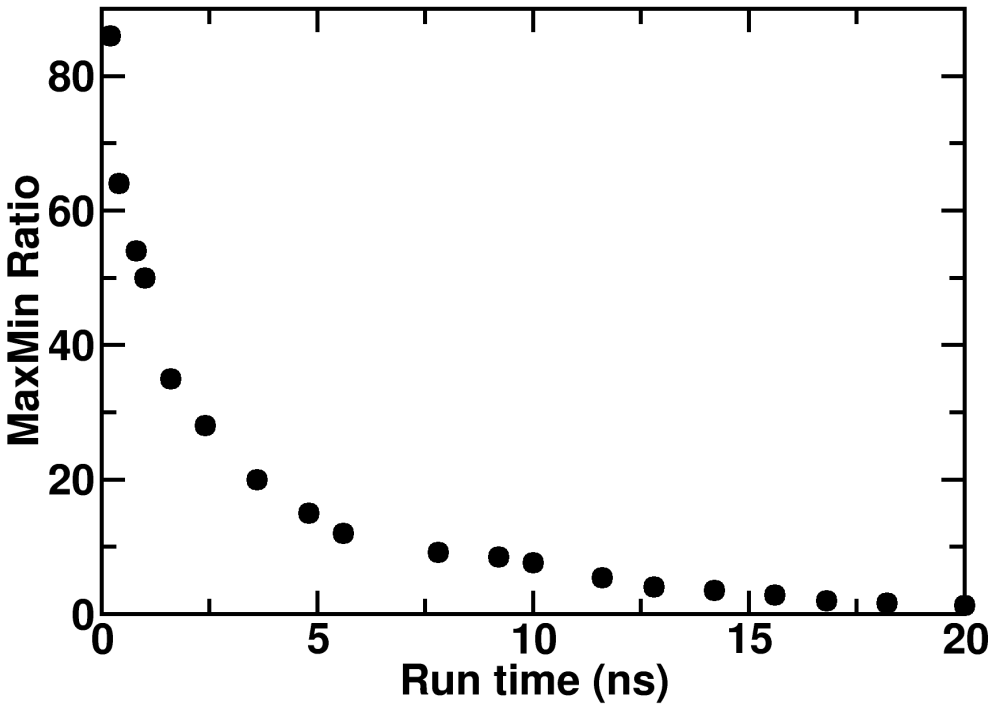

Fig. S10 Evolution of the MaxMin ratio for graphene in [bmim][NTf_2] during a 20 ns ABF-MD simulation.

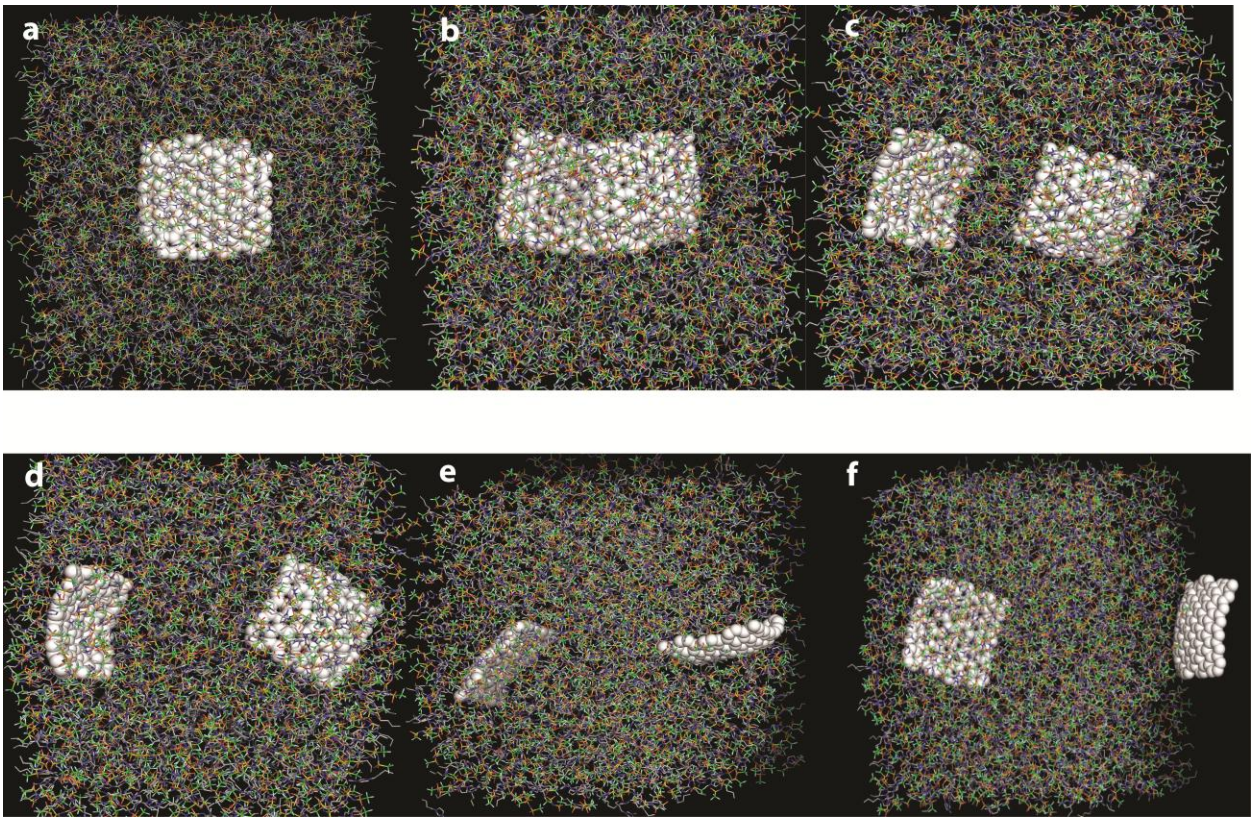

Fig. S11 Progressive snapshots of graphene exfoliation from a bilayer (in the *z* direction) in [bmim][NTf_2] during ABF simulation at 300 K.

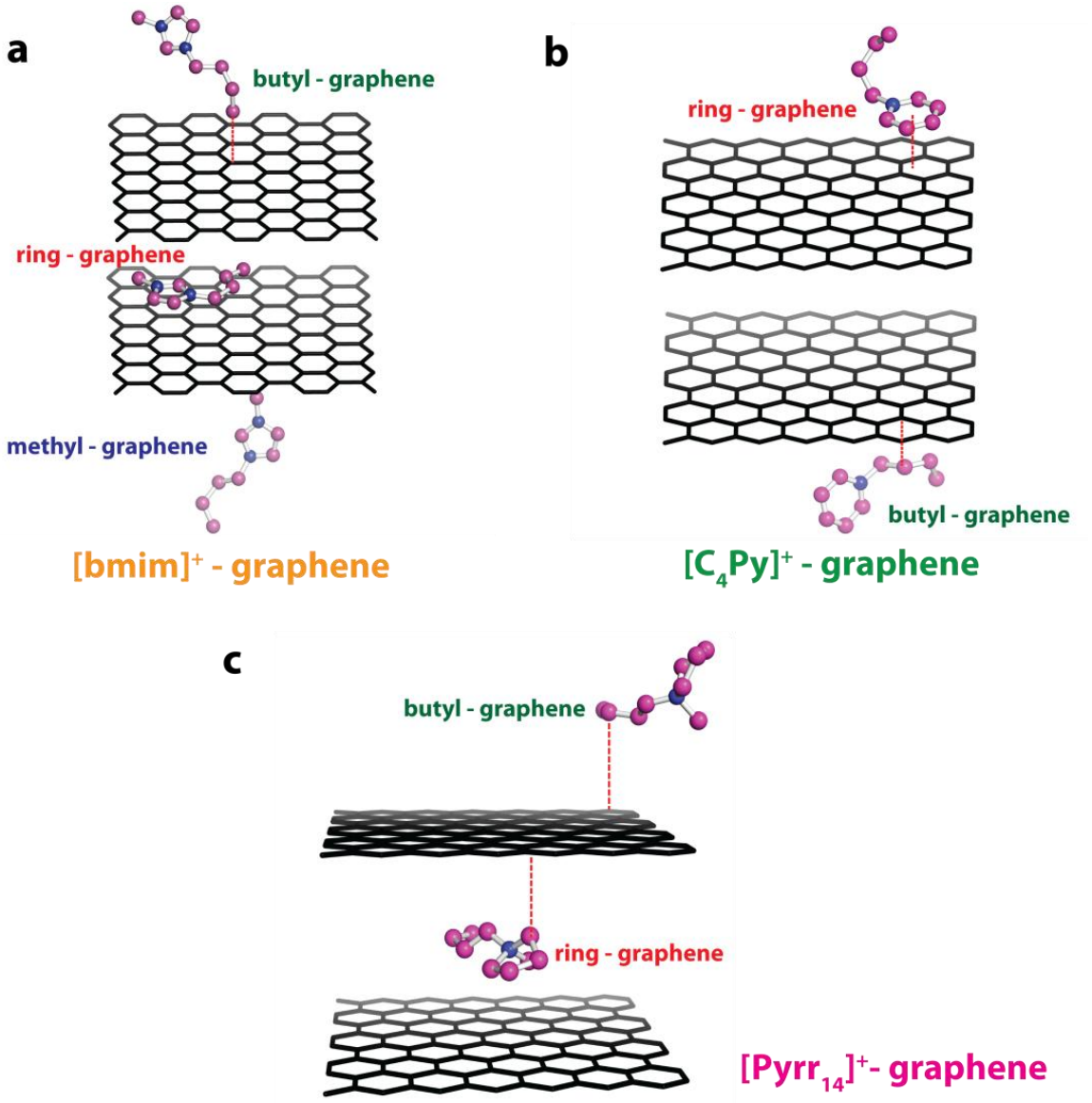

Fig. S12 Illustrative examples of different interactions possible between the IL cations studied and the graphene surface.

Table S1: Single point calculations using B3LYP/6-31+g(d,p) level of theory (Gaussian 09)[S1] for conformations of different IL interactions with the graphene bilayer, see Fig. S8.

Cation + graphene	Energy (a.u)	ΔE (kcal mol^{-1})
[bmim]$^+$		
methyl carbon	–4687.80703122	9.27
butyl carbon	–4687.82183670	0
ring (π–π)	–4687.80694225	9.34
[Pyrr$_{14}$]$^+$		
butyl carbon	–4674.14508420	0
ring	–4674.12088704	15.20
[C$_4$Py]$^+$		
ring (π–π)	–4670.59938589	0
butyl carbon	–4670.58381349	9.77

General Methods

Adaptive biasing force (ABF) method is a technique developed by Darve *et al.* [S2-4] to calculate the free energy difference of certain chemical or biological processes along generalized reaction coordinates in the system of interest. This method is a combination of probability density and constraint force methods, and is based on the thermodynamic integration of average force acting on coordinates, which is unconstrained.[S2] As a part of ABF algorithm, an external biasing force, estimated locally from the sampled conformations of the system and updated continuously, is applied at each step to facilitate the system in overcoming significant energy barriers along the reaction coordinate. This allows the system to evolve freely without constraints, enabling the simulation to visit multiple states separated by high free energy barriers and improving sampling long the reaction coordinate. The theoretical foundation of this method is based on Equation 1, which is a modified version of the expression proposed by Darve and Pohorille[S2, S3] for the effective force (F^u) acting on the reaction coordinate (ξ),

$$F_{\xi}^{u} = m_{\xi}\frac{d^2\xi}{dt^2} + \frac{1}{\beta}\sum_{k=1}^{3M}\frac{1}{m_k}\frac{d\xi}{dx_k}\frac{dm_{\xi}}{dx_k} \qquad (1)$$

where m_k are generalized masses associated with generalized coordinates represented by x_k.

The average of this applied force is equal and opposite to the mean force acting on ξ and cancels the free energy derivative computed for small intervals of reaction coordinate ξ so that the system can evolve and overcome free energy barriers.

$$\langle \frac{\partial H}{\partial \xi} \rangle_{\xi} = -\langle F_{\xi}^{u} \rangle_{\xi} \quad \textbf{(2)}$$

The Helmholtz free energy $\boldsymbol{A}$ at constant temperature T, constant volume V and number of particles N is given by:

$$A(N,V,T) = -k_b T \log Z(N,V,T) \quad \textbf{(3)}$$

where $\boldsymbol{Z}$ is the canonical partition function and $\boldsymbol{k_b}$ is the Boltzmann's constant.

The free energy as a function of the reaction coordinate can be written as:

$$A(N,V,T,\xi) = -k_b T \log \frac{\int \exp[-\beta H(x,p)] \delta(\xi(x) - \xi_o) dx\, dp}{\Lambda^{3M} N!} \quad \textbf{(4)}$$

where Λ is the thermal wavelength and p is the conjugate momenta of position coordinate x.

It is more convenient to compute the free energy difference $\Delta \boldsymbol{A_{a \to b}}$ between state A and B for a system. The states A and B are based on the reaction coordinate which is a function of the particle position.

$$\Delta A_{a \to b} = \int_{\xi_a}^{\xi_b} \frac{dA(\xi)}{d\xi}\, d\xi \quad \textbf{(5)}$$

The first derivative of the free energy is related to the partial derivative of the Hamiltonian of the system with the reaction coordinate[S5] and therefore based on Equation **5** can be related to the constraint force acting along the reaction coordinate

$$\Delta A_{a \to b} = \int_{\xi_a}^{\xi_b} \frac{dA(\xi)}{d\xi}\, d\xi = \int_{\xi_a}^{\xi_b} \langle \frac{dH(\xi)}{d\xi} \rangle_{\xi}\, d\xi = \int_{\xi_a}^{\xi_b} -\langle F_{\xi}^{u} \rangle_{\xi}\, d\xi \quad \textbf{(6)}$$

Further details of the ABF method and formulation including the implementation in NAMD[6] molecular dynamics package can be found in these publications.[S2-5, S7-10] The Helmholtz free energy $\boldsymbol{A}$ obtained from NVT ensemble simulations is in close approximation to the Gibbs free energy $\boldsymbol{G}$ in condensed phase.[S11] The Gibbs free energy difference is used to compute the free energy of solvation of graphene sheets in water and ILs.

Intermolecular Potential

The force field developed by Lopes and co-workers based on the OPLS/AMBER framework was used to model the dialkylimidazolium,[S12, S13] N-butylpyridinium, [S14] tetra-butylphosphonium [S14] cation and anion [NTf_2]. [S15, S16] This force field for ionic liquids is based on the 12-6 Lennard Jones model and unity point charges and predicts the pure component thermodynamic properties in good agreement with experiment. The force field for graphene sheet was based on the parameters from Patra *et al.* [S17] The force field is also based on the 12-6 potential, therefore making it easy to use the combining rules for non–bonded interactions of graphene with IL or water. The R_{min} of the carbon is set at 3.98 Å while the well depth of the carbon is 0.07 kcal mol^{-1}. The carbon–carbon bond stretching force constant is set at 322.55 kcal mol^{-1}, angle bending constant at 53.35 kcal mol^{-1} and torsional force constant at 3.15 kcal mol^{-1}.

Simulation Details

A rectangular simulation cell was used, with dimensions 80 Å × 80 Å × 200 Å, with the condensed phase occupying a region approximately 80 Å × 80 Å × 80 Å. This cell was extended to 200 Å in the *z*–direction with a 120 Å vacuum region. The vacuum region is necessary to prevent interactions of the solute with the condensed phases through periodic boundary conditions. The number of molecules in each box was selected to reproduce the density of the ionic liquid as predicted by *NPT* simulations at 1 atm and 300 K for a specific potential truncation (14 Å). The reaction coordinate for the determination of free energy changes was defined as the distance between the center of mass of the graphene sheet (COMS) under study and center of mass of the condensed phase (COMCP). In the initial system setup, the COMS was placed at approximately the COMCP. Over the course of simulation, the reaction coordinate spanned a distance of 120.0 Å from the center of mass of the condensed phase to the center of the vacuum region. To reduce the statistical error of the calculations, the reaction pathway was divided into eighteen equally sized non–overlapping windows of 5.0 Å. To generate the initial configurations for each window, a single 20 ns ABF run was performed spanning the complete reaction pathway from 0.0 Å to 90.0 Å after heating and equilibration of the system. Coordinates from the trajectory of this simulation were saved periodically to generate eighteen initial coordinate files for the five windows. Force statistics were stored in bins of width 0.05 Å. The biasing force was applied after 500 samples were collected in each bin. To keep the solute within the specified window, a harmonic force with a magnitude of 10.0 kcal mol^{-1} $Å^{-1}$ was applied on the upper and lower boundary of the window along the *z*-axis of the simulation cell. A final production run of 30 ns for each window was performed.

Molecular dynamics simulations were performed with NAMD version 2.7b3.[S6] Initial configurations for each system were generated with Packmol.[S18] Energy minimization was performed on all systems for 500 steps using the steepest decent technique. Systems were equilibrated over a time period of 2.0 ns in isobaric–isothermal ensemble at 1.0 atm and 300 K, followed by the ABF–MD calculation in NVT ensemble. For all calculations, the temperature was maintained at 300 K using Langevin dynamics. For initial *NPT* simulations, used to

determine the density of each system, constant pressure was maintained at 1.0 atm using the Nose–Hoover algorithm.[S19, S20] A timestep of 2.0 fs was used for the integration of Newton's equation of motion. Periodic boundary conditions were used in all the three spatial coordinates. Long range electrostatic interactions were calculated with particle–mesh Ewald algorithm.[S21, S22] A switching function was applied for all Lennard–Jones interactions at 12.5 Å for 14.0 Å cut-off. Data were analysed using VMD. [S23]

References

S1 R. A. Gaussian 09, M. J. Frisch, G. W. Trucks, H. B. Schlegel, G. E. Scuseria, M. A. Robb, J. R. Cheeseman, G. Scalmani, V. Barone, B. Mennucci, G. A. Petersson, H. Nakatsuji, M. Caricato, X. Li, H. P. Hratchian, A. F. Izmaylov, J. Bloino, G. Zheng, J. L. Sonnenberg, M. Hada, M. Ehara, K. Toyota, R. Fukuda, J. Hasegawa, M. Ishida, T. Nakajima, Y. Honda, O. Kitao, H. Nakai, T. Vreven, J. A. Montgomery, Jr., J. E. Peralta, F. Ogliaro, M. Bearpark, J. J. Heyd, E. Brothers, K. N. Kudin, V. N. Staroverov, R. Kobayashi, J. Normand, K. Raghavachari, A. Rendell, J. C. Burant, S. S. Iyengar, J. Tomasi, M. Cossi, N. Rega, J. M. Millam, M. Klene, J. E. Knox, J. B. Cross, V. Bakken, C. Adamo, J. Jaramillo, R. Gomperts, R. E. Stratmann, O. Yazyev, A. J. Austin, R. Cammi, C. Pomelli, J. W. Ochterski, R. L. Martin, K. Morokuma, V. G. Zakrzewski, G. A. Voth, P. Salvador, J. J. Dannenberg, S. Dapprich, A. D. Daniels, Ö. Farkas, J. B. Foresman, J. V. Ortiz, J. Cioslowski, and D. J. Fox., *Gaussian, Inc., Wallingford CT, 2009.*, (2009).
S2 E. Darve and A. Pohorille, *J. Chem. Phys.*, 2001, **115**, 9169-9183.
S3 E. Darve, M. A. Wilson and A. Pohorille, *Mol. Simul.*, 2002, **28**, 113-144.
S4 D. Rodriguez-Gomeza, E. Darveb and A. Pohorille, *J. Chem. Phys.*, 2004, **120**, 3563.
S5 E. Darve, David Rodríguez-Gómez and A. Pohorille, *J. Chem. Phys.*, 2008, **128**, 144120.
S6 J. C. Phillips, R. Braun, W. Wang, J. Gumbart, E. Tajkhorshid, E. Villa, C. Chipot, R. D. Skeel, L. Kale and K. Schulten, *J. Comput. Chem.*, 2005, **26**, 1781-1802.
S7 C. Chipot and J. Henin, *J. Chem. Phys*, 2005, **123**.
S8 J. Henin and C. Chipot, *J. Chem. Phys.*, 2004, **121**, 2904-2914.
S9 J. Henin, G. Fiorin, C. Chipot and M. L. Klein, *J. Chem. Theor. Comput.*, 2010, **6**, 35-47.
S10 C. Chipot and A. Pohorille, *Free Energy Calculations*, Springer, 2007.
S11 M. Buhl and G. Wipff, *ChemPhysChem*, 2011, **12**, 3095-3105.
S12 J. N. C. Lopes, J. Deschamps and A. H. Padua, *J. Phys. Chem. B*, 2004, **108**, 2038-2047.
S13 J. N. C. Lopes, J. Deschamps and A. H. Padua, *J. Phys. Chem. B*, 2004, **108**, 11250.
S14 J. N. C. Lopes and A. H. Padua, *J. Phys. Chem. B*, 2006, **110**, 19586-19592.
S15 J. N. C. Lopes and A. H. Padua, *J. Phys. Chem. B*, 2004, **108**, 16893-16898.
S16 K. Shimizu, D. Almantariotis, M. F. Costa Gomes and J. N. C. Lopes, *J. Phys. Chem. B*, 2010, **114**, 3592-3600.
S17 N. Patra, B. Wang and P. Kral, *Nano Lett.*, 2009, **9**, 3766-3771.
S18 L. Martinez, R. Andrade, E. G. Birgin and J. M. Martinez, *J. Comput. Chem.*, 2009, **30**, 2157-2164.
S19 S. E. Feller, Y. H. Zhang, R. W. Pastor and B. R. Brooks, *J. Chem. Phys.*, 1995, **103**, 4613-4621.
S20 G. J. Martyna, D. J. Tobias and M. L. Klein, *J. Chem. Phys.*, 1994, **101**, 4177.
S21 T. Darden, D. York and L. Pedersen, *J. Chem. Phys.*, 1993, **98**, 10089-10092.
S22 U. Essmann, L. Perera, M. L. Berkowitz, T. Darden, H. Lee and L. G. Pedersen, *J. Chem. Phys.*, 1995, **103**, 8577-8593.
S23 W. Humphrey, A. Dalke and K. Schulten, *J. Mol. Graphics*, 1996, **14**, 33.